

This document is the pre-print version of the manuscript
Ricci, M., Silipigni, G., Ferrigno, L., Laracca, M., Adewale, I. D., & Tian, G. Y. (2017). Evaluation of
the lift-off robustness of eddy current imaging techniques. *NDT & E International*, 85, 43-52.
DOI: <https://doi.org/10.1016/j.ndteint.2016.10.001>

Experimental evaluation of the robustness of Eddy Current Imaging techniques against Lift-off variations.

Marco Ricci^{1*}, Giuseppe Silipigni¹, Luigi Ferrigno², Marco Laracca², Ibukun D. Adewale^{1,3}, Gui Yun Tian³

¹Dipartimento di Ingegneria, Polo Scientifico Didattico di Terni, Università di Perugia,

Strada di Pentima 4, 05100 Terni, Italy

marco.ricci@unipg.it, giuseppe_silipigni@hotmail.com

²Dipartimento di Ingegneria Elettrica e dell'Informazione, Università degli Studi di Cassino e del Lazio Meridionale,

Via G. Di Biasio 43, 03043, Cassino (FR) Italia

ferrigno@unicas.it, m.laracca@unicas.it

³School of Electrical and Electronic Engineering, Newcastle University,

Newcastle upon Tyne NE1 7 RU, UK

ibukun.adewale@newcastle.ac.uk, g.y.tian@newcastle.ac.uk

***Abstract*— The development of lift-off invariant strategies is one of the main goals in Eddy Current Non-Destructive Testing research. In the present work, two imaging procedures based on the measurement and analysis of amplitude and phase signals of magnetic field sensors and suitably developed for Multi-Frequency Eddy Current Testing are analyzed and compared with respect to their ability to retrieve reliable results even in presence of huge changes of lift-off. A figure of merit based on the Signal to Noise Ratio evaluated on the 2D reconstructed images is used to quantitatively**

compare the different strategies in terms of defect image quality. The numerical and experimental analysis carried out show that imaging procedures relying on the analysis of the phase-lag are quite insensitive changes in the lift-off and that they even guarantee good results when the probe lift off is randomly changed on each point of the scanned map with variations up to 3 mm. On the other hand imaging procedures based on the visualization of amplitude-derived features are able to tolerate only lift-off fluctuation lower than 1mm. In addition the paper also show that by exploiting the analysis of the images' SNR at different frequencies, some insight on the defect depth can be gained even in the case of huge lift-off variation among the different position of the scanning probe.

Keywords—Eddy Current Testing, Image Processing, Lift-off invariance

I. INTRODUCTION

Eddy Current Non Destructive Testing and Evaluation (ECT) is widely used in many industry sectors to inspect and assess the integrity of conductive structures. Besides the inspection of metallic samples for which ECT has been applied for some decades to detect cracks, voids, corrosion and other defect typologies structures [1-4], ECT is more and more used also for the analysis of conductive composites materials based on Fiber-Carbon-Reinforced-Plastic to analyze fiber integrity, their spatial distribution, etc. [5-6].

Increasingly, in most recent years ECT has also been used in conjunction with Thermography to detect defects in conductors [7-9] and for Structural Health Monitoring (SHM) applications based on embedded eddy current (EC) sensors [10].

The sensitivity of ECT for certain class of defects such as small surface or near-surface cracks is very high, far superior to other NDT techniques (X-ray, Ultrasonic, etc.), but at the same time this high sensitivity presents drawbacks that yet hamper inspections and analysis.

Among these, lift-off (LO) variation is cardinal for various field realities. Indeed the variation of the mutual distance between the exciting probe and the sample under inspection leads to a change of the eddy currents distribution inside the material and hence a change of the signal received by the sensor, which can consist of the same excitation coil, a distinct pick-up coil, a B-field sensor such as Giant Magneto Resistance–GMR- or Hall probes, or a Magneto-Optic camera [1-4, 11]. Several strategies have been proposed to mitigate the effect of LO variation on ECT signals: design of particular excitation/receiving coil [12], the exploitation of peculiar invariance properties of ECT measurements, and the development of signal processing algorithms [13-16].

This paper focuses on the effect of LO variation on ECT imaging techniques applied to the detection of small sub-surface and inner cracks in Aluminium samples. Such defects are of interest for aerospace industry where Aluminium is still one of the most used materials for his low density and good mechanical performances and can be extended to many others metallic materials and application fields. In particular, starting from recent results of some of the present authors [17-18], a suitable MF signals has been defined and two ECT imaging procedures derived by multi-frequency ECT test (MF-ECT) are compared in order to identify the more robust one with respect to LO variation.

MF-ECT is one of most used ECT techniques since it assures a relative easy experimental implementation and information extraction: taking into account the physics of eddy current, and the concept of skin depth, each tone is associated to a different inspection depth and by collecting data at different frequencies/depths, various analysis protocols can be used to both detect the presence of a defect and extract some estimates about its physical and geometrical characteristics [11,17-21].

To cite a few, we mention multi-frequency (MF) impedance plane analysis, neural network and other classification methods, deterministic inversion procedures referring the readers to the extensive literature on the subject.

As a matter of fact, most of the MF-ECT applications to defect detection and characterization have exploited and processed the information enclosed in the amplitudes of the tones. Nevertheless, the information provided by MF-ECT is inherently twofold: each tone is completely characterized by amplitude and phase.

This paper aims at analyzing the robustness of amplitude and phase parameters retrieved by ECT imaging and identifying the most robust one with respect to LO variations. Precisely, the paper aims in comparing the performance of crack detection and characterization for both the amplitude-based and phase-based imaging in presence of different lift off finally considering an extreme case characterized by a ECT probe with random LO applied during the image acquisition. To perform this comparison a suitable and well assessed figure of merit is adopted during in the tests [18]. The aim is to show the extreme robustness of the phase-based imaging procedure with respect LO random variation, whereas amplitude-based one becomes rapidly ineffective as the LO variations increase.

The rest of the paper is organized as follows: Section II briefly reviews the ECT theory and introduce through semi-analytics and numerical simulations why the phase is expected to be more robust against LO variations. Section III introduces the measurement procedure and the image formation strategies used in the analysis while Section IV reports the experimental result and the comparison between the various imaging techniques. Section V draws conclusion and future perspectives.

II. THEORETICAL BACKGROUND AND NUMERICAL SIMUATIONS

The Eddy-Current Non Destructive Testing method relies basically on Faraday's law of electromagnetic induction and the physics of ECT is thus regulated by Maxwell Equations. In particular, due to the low frequencies of operation, and the dimensions of the experimental set-up, the displacement current term can be neglected and the so-called quasi-static approximation can be adopted [22]:

$$\nabla \cdot \mathbf{D} = \rho; \nabla \cdot \mathbf{B} = 0; \nabla \times \mathbf{E} = -\partial \mathbf{B} / \partial t; \nabla \times \mathbf{H} = \mathbf{J}; \quad (1)$$

By considering an isotropic, homogenous non-magnetic metallic material for which the constitutive relations are:

$$\rho = 0; \mathbf{D} = \epsilon \mathbf{E}; \mathbf{J} = \sigma \mathbf{E}; \mathbf{B} = \mu \mathbf{H} \quad (2)$$

\mathbf{E}, \mathbf{B} and \mathbf{J} inside the material are governed by the following diffusion equations:

$$\frac{\partial \mathbf{E}}{\partial t} - \alpha \nabla^2 \mathbf{E} = \mathbf{0}; \frac{\partial \mathbf{H}}{\partial t} - \alpha \nabla^2 \mathbf{H} = \mathbf{0}; \frac{\partial \mathbf{J}}{\partial t} - \alpha \nabla^2 \mathbf{J} = \mathbf{0} \quad (3)$$

where $\alpha = 1/\mu\sigma$ is the magnetic diffusivity, defined in analogy with the thermal diffusivity.

For single frequency excitation, Eqs.(3) can be re-written in the phasor form and in particular the 1D steady-state solution of the current density equation in the case of a sheet of alternating current density at the surface of a semi-infinite medium is given by the following relation, where the overbar indicates phasor quantities.:

$$\frac{d^2 \bar{J}}{dz^2} = j \frac{\omega}{\alpha} \bar{J}. \quad (4)$$

As well known, Eq. (4) does not describe propagating waves but instead the diffusion of the eddy current inside the materials whose amplitude decays exponentially and whose phase increases linearly with depth:

$$\bar{J}(z, t) = \bar{J}(0, t) e^{-\frac{z}{\delta}} e^{j(\omega t - \frac{z}{\delta})} = |\bar{J}(z, t)| e^{j(\omega t - \Phi(z))}; \quad (5)$$

$$|\bar{J}(z, t)| = |\bar{J}(0, t)|e^{-z/\delta}; \Phi(z) = \sqrt{\frac{\omega}{2\alpha}}z; \delta = \sqrt{\frac{2\alpha}{\omega}} = \sqrt{\frac{2}{\omega\mu\sigma}}$$

In the previous equation, δ is the skin depth and, for a given frequency, both the diffusivity α , and hence the penetration speed, and the skin depth decrease as conductivity and permeability of the material increase.

Analogous to the propagation of heat in a semi-infinite conductive medium [23], one can also define the phase velocity $v_{\text{eddy}} = \omega\delta = \sqrt{2\alpha\omega}$. Although there is no propagation of waves, phase velocity gives a useful insight since it establishes that diffusion is also dispersive. Different frequencies “travel” with different velocities, higher frequencies diffuse more rapidly with shallower depths, whilst lower frequencies have higher penetration depths with longer diffusion times.

In real applications, the sample has finite dimensions and the excitation coil consists of several windings oriented parallel or perpendicular to the sample surface, as in the present case. The solutions of Eq.4 are thus more complex but Eqs. 5 still hold provided that the skin depth δ is replaced with an “effective” one δ_{eff} [24-25] and that $\bar{J}(0, t)$ is replaced by a 2D distribution of the current density $\bar{J}(x, y, z=0, t)$ on the surface of the sample. δ_{eff} can be calculated analytically or numerically but it is not strictly necessary for the present results, it is enough to know that the eddy current density decreases exponentially with z and that the time of diffusion depends on the excitation frequency.

Conversely, in the light of the following discussion the key point is: how do lift-off variations affect the distribution of the eddy-current in the material? Or in other words, how $|\bar{J}(x, y, z, t)|$ and $\Phi(x, y, z, t)$ depend on the lift-off value?

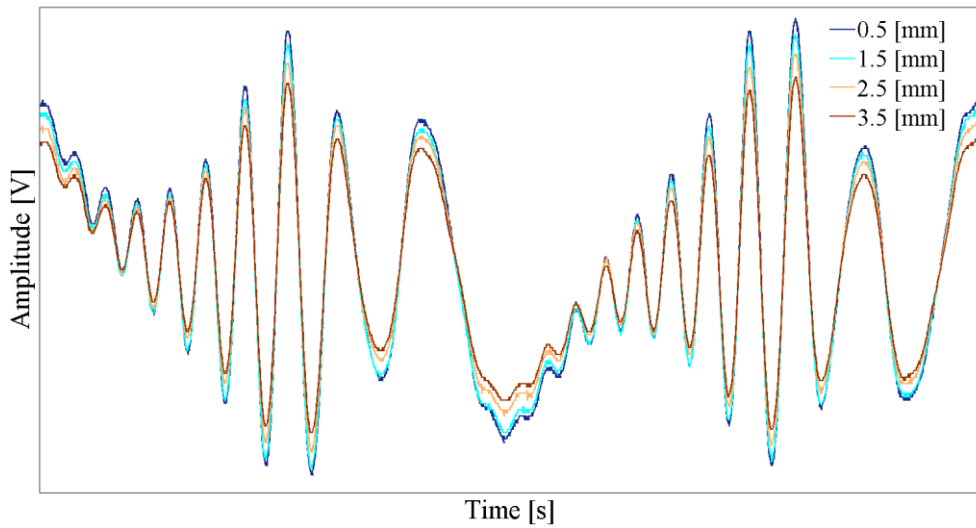


Figure 2. Example of the output of the GMR probe acquired on a sound point of the sample for 4 different LO values.

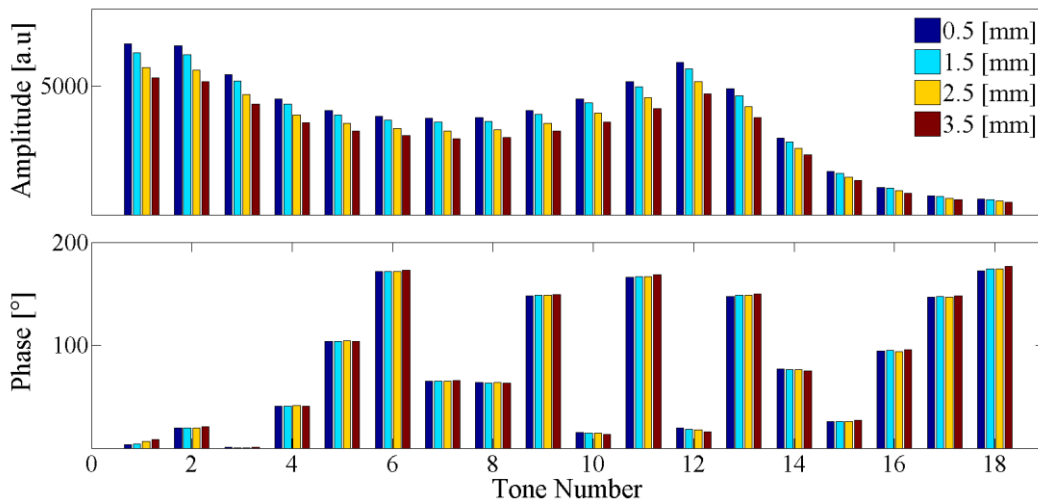


Figure 3 Bar-chart of the amplitude (top) and phase (bottom) of the N_f tones composing the MF signals acquired for the 4 different LO values reported in Figure 2.

frequency domain, illustrated in Figure 3. The bar-chart reports values of amplitude and phase of the N_f frequencies composing the MF signals for the four considered LOs. Also this analysis confirm that the amplitudes of the various tones are strongly affected by the lift-off, while the phase lags are weakly affected by the LO variations.

Intuitively, the robustness of the phase approach could be expected by considering the equations introduced above. Indeed in the air between coil and sample, the solution of Maxwell equations are propagating waves with phase velocity equal to c (that is the speed of light in vacuum) and with wavelength $\lambda=c/f$; inside the material the phase velocity is

$v_{\text{eddy}} = \omega\delta = \sqrt{2\alpha\omega}$ and the resulting “effective” wavelength is $\lambda_{\text{eddy}} = v_{\text{eddy}} / f = 2\pi\delta$ so that the diffusion over a distance $d=\delta$ causes a phase shift of 2π . The ratio between phase velocity in air and inside the conductive sample is:

$$\eta = \frac{c}{v_{\text{eddy}}} = \frac{\lambda}{\lambda_{\text{eddy}}} = \frac{c}{\sqrt{2\alpha\omega}} = \frac{\sqrt{\mu\sigma c^2}}{2\sqrt{\pi f}} = \frac{\sqrt{\mu\sigma}}{2\sqrt{\pi\varepsilon_0\mu_0 f}} \sim \frac{\sqrt{\sigma}}{2\sqrt{\pi\varepsilon_0 f}} = \frac{5.73 \times 10^8}{\sqrt{f}} \quad (6)$$

For the frequency values used in this paper (from 540 to 54000 Hz), η falls in the interval from 10^6 to 10^7 . If we consider the \mathbf{B} field measured in the proximity of the sample surface due to the sum of two contributors, $\mathbf{B} = \mathbf{B}_0 + \mathbf{B}_{\text{eddy}}$, with \mathbf{B}_0 being the field without the sample and \mathbf{B}_{eddy} that due to eddy currents, it can be assumed that the phase of \mathbf{B}_{eddy} is almost due to diffusion of eddy current inside the material and it is pretty invariant with respect to variations of the position of the B-field sensor. This assumption is confirmed by the fact demonstrated in [27-30] that changes in the normalized impedance of ECT excitation coil exhibit a constant phase angle at different LO values. Conversely, even small changes in LO value strongly affect the amplitude of the eddy current density in the sample $|\bar{\mathbf{J}}(x, y, z, t)|$ and thus \mathbf{B}_{eddy} . By designing coils that assure the independence of \mathbf{B}_0 from LO [31-32], or providing as in this case a constant excitation current waveform regardless of the lift-off value, makes the phase of \mathbf{B} pretty immune to lift-off variations.

Starting from these preliminary results the paper aims to quantitatively analyze the robustness of the phase-based imaging procedure respect to the amplitude-based one.

III. ECT SIGNAL AND IMAGE PROCESSING

A. Excitation Signals and Measured Output

The ECT excitation is a Multi-Frequency signal $S_{\text{IN}}(t)$ realized by combining N_f sinusoidal tones chosen to excite the selected frequency components $\{f_k\}$'s with the desired amplitudes $\{a_k\}$'s and phases $\{\varphi_k\}$'s:

$$s_{IN}(t) = \sum_{k=1}^{N_f} a_k \sin(2\pi f_k t + \varphi_k) \quad (7)$$

While the $\{a_k\}$'s determine the power spectrum of $S_{IN}(t)$, the phases $\{\varphi_k\}$'s affect the envelope and then its peak factor. In this paper, $\{\varphi_k\}$'s follow the rule derived by Schroeder [33] that assures the minimal peak-factor for linear spaced multi-frequency signals, that is when all the $\{f_k\}$'s are multiples of a fundamental one, even in the case of arbitrary $\{a_k\}$'s. This is the case of the present work where $f_k = (2k-1)f_0$ with $f_0=1500\text{Hz}$ and $k \in [1, N_f=18]$; at the same time the amplitudes of the various tones are all equal to assure the same energy at each frequency. The minimization of the peak factor implies an optimization of the SNR of the measurement, especially when the finite number of bit of any Analog-to-Digital Converter used to measure the output signal is considered [34].

The output signal $S_{OUT}(t)$ consists of the voltage output of the GMR-based probe proportional to the B component (see Figures 1) and it is expressed by:

$$s_{OUT}(t) = \sum_{k=1}^{N_f} A_k \sin(2\pi f_k t + \Phi_k) \quad (8)$$

B. Image Formation

Starting from the measurement of $S_{OUT}(t)$ on a regular grid of points with coordinates $(\{x_l\}, \{y_m\})$, two image procedures are compared relying on amplitude and phase feature respectively. In detail, at first a set of N_f images is obtained by visualizing for every tone and for each point the value of coefficient A_k defined in Eq. 8.

$$IM_{MF}M(f_k, x_l, y_m) = A_k(x = x_l, y = y_m); \{k \in [1, N_f], l \in [1, N_x], m \in [1, N_y]\} \quad (9)$$

Then a set of N_f images is obtained by visualizing for every tone and for each point the value of coefficient Φ_k defined in Eq. 8.

$$IM_{MFP}(f_k, x_l, y_m) = \Phi_k(x = x_l, y = y_m); \{k \in [1, N_f], l \in [1, N_x], m \in [1, N_y]\} \quad (10)$$

$2 \times N_f$ images corresponding to different penetration depths are then built-up and they exhibit different sensitivities and different spatial resolution with respect to defects of varying

depths. By analyzing the various images with the image processing procedure described below; for each defect an optimal image can be selected from which some indications about defect depth can be argued.

The procedures require extremely light computational power and it must be stressed that they do not require also the use of a sound point as a reference, which represents a drawback in on-field measurements and an extra-computational cost.

To study and compare the two imaging procedures with respect to the variation of lift-off in a *wide variety of possible real situations a set of scans have been acquired for each analyzed defect*. Four different values of the lift-off parameter $LO \in \{0.5\text{mm}, 1.5\text{mm}, 2.5\text{mm}, 3.5\text{mm}\}$ have been considered. This can be summarized by introducing the parameter LO in the Eqs. 9 and 10 so that as example $IM_{MFM}(f_k, x_l, y_m, LO_n)$ denotes the set of N_f images obtained for the lift-off value LO_n . Starting from these data, various possible sources and types of lift-off variations have been simulated, as explained in the next subsections

C. Image Formation with point-by-point random lift-off variation.

To stress the effect of the lift-off variation a worst case represented by the presence of randomised lift-off has been considered. To this aim a random variation of the lift-off among the four available values has been applied on each point (x_l, y_m) . This worse situation models the effect on measurements of “high-frequency” vibrations of the ECT probe during the translation stage.

Various intensities of lift-off randomness have been simulated by letting the LO parameter to vary among the set of values with pre-fixed probability distributions.

In the configuration LO_{R1} the LO varies randomly with uniform probability among the two smallest values, that is $\{p(LO=0.5\text{mm})=1/2, p(LO=1.5\text{mm})=1/2\}$, then in the other configurations the lift-off “randomness” is increased step-by-step. Precisely in the

configuration LO_{R2} , LO varies with the probability distribution $\{p(LO=0.5mm)=1/3, p(LO=1.5mm)=1/3, p(LO=2.5mm)=1/3\}$; in LO_{R3} LO assumes randomly one of the 4 values $\{p(LO=0.5mm)=1/6, p(LO=1.5mm)=1/3, p(LO=2.5mm)=1/3, p(LO=3.5mm)=1/6\}$, in LO_{R4} LO assumes randomly one of the 4 values $\{p(LO=0.5mm)=1/4, p(LO=1.5mm)=1/4, p(LO=2.5mm)=1/4, p(LO=3.5mm)=1/4\}$.

The images obtained are denoted as $IM_{MF}M(f_k, x_l, y_m, LO \in LO_{Rp})$ and $IM_{MF}P(f_k, x_l, y_m, LO \in LO_{Rp})$ respectively.

D. Image Formation with arbitrary lift-off variation.

Point-by-point random lift-off variations represent a good test for evaluating the robustness of imaging procedures. Nonetheless, variation of lift-off can originate from many other sources, which includes the curvature of the sample or the not-perfect alignment between sample and sensor.

To simulate such cases, a finer variation of LO is necessary. To do this by avoiding a huge experimental effort, we interpolated the experimental data $S_{OUT}(t, x_l, y_m, LO_n)$ acquired at different LO 's values in order to simulate intermediate variations of lift-off (e.g. $S_{OUT}(t, x_l, y_m, LO=1.25mm) = 0.25 S_{OUT}(t, x_l, y_m, LO=1.25mm) + 0.75 S_{OUT}(t, x_l, y_m, LO=1.25mm)$)

In general, the change of $s_{OUT}(t)$ is not expected to be linear with LO but we verified on experimental data that this approximation is very reasonable for the present set-up. We believe this is due to the small interval of interpolation (1mm) and to the almost independence of the phase from LO 's value, see Figure 4. By adopting this strategy, parabolic, saddle-shaped, etc curved surface/ lift-off trajectories have been simulated as well as linear drifts. It is worth stressing that the latter case can also represent the effect of a thermal drift in the measurement chain, then extending the robustness evaluation to other relevant noise and error sources.

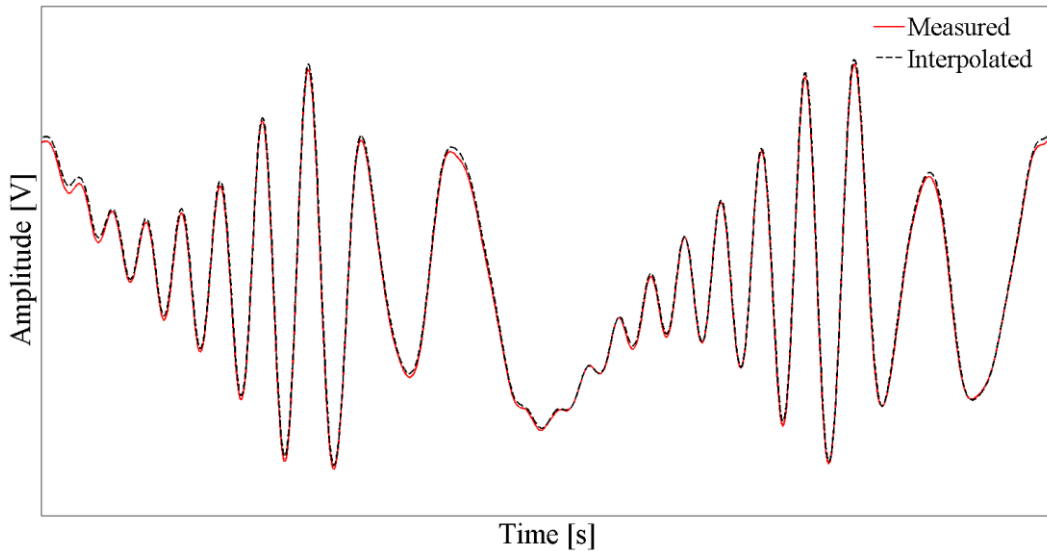


Figure 4. Comparison between: (solid red) experienced GMR-based probe response $S_{OUT}(t)$ measured at a sound point of the sample for $LO=1.5\text{mm}$; (dashed black) and a simulated one obtained by interpolating $S_{OUT}(t)$ at $LO=0.5\text{mm}$ and $S_{OUT}(t)$ at $LO=2.5\text{mm}$. The deviation of the interpolated data from the experimental one is very small.

E. Image processing

The images produced with the aforementioned procedures present different ranges of intensities due to the different quantities visualized and moreover are affected by unwanted noisy components. In particular the images' noise can be modeled as a low-spatial frequency noise caused by drifts in the measurement station and by a high-frequency noise (salt&pepper noise) due to electrical environmental noise. To reduce the noise in the images, in [18] a denoising algorithm has been introduced and here applied. Also, in the same work [18] an adimensional SNR parameter has been assigned to each image quantifying the “visibility” of the typical defects pattern. Henceforth, the same SNR parameter is adopted in the analysis of the experimental data. The SNR parameter is twofold useful: (1) the analysis of the SNR values at different frequencies - $SNR(f_k)$ - allows the optimal frequency of inspection f^* to be determined; (2) the comparison of the SNR values achieved at f^* by IM_{MFA} and IM_{MFP} allows the optimal image procedure in terms of defect detection to be established.

f^* in general is different for amplitude and phase analysis and, since the frequency of inspection is related to the spatial distribution of the eddy current inside the sample, f^* is

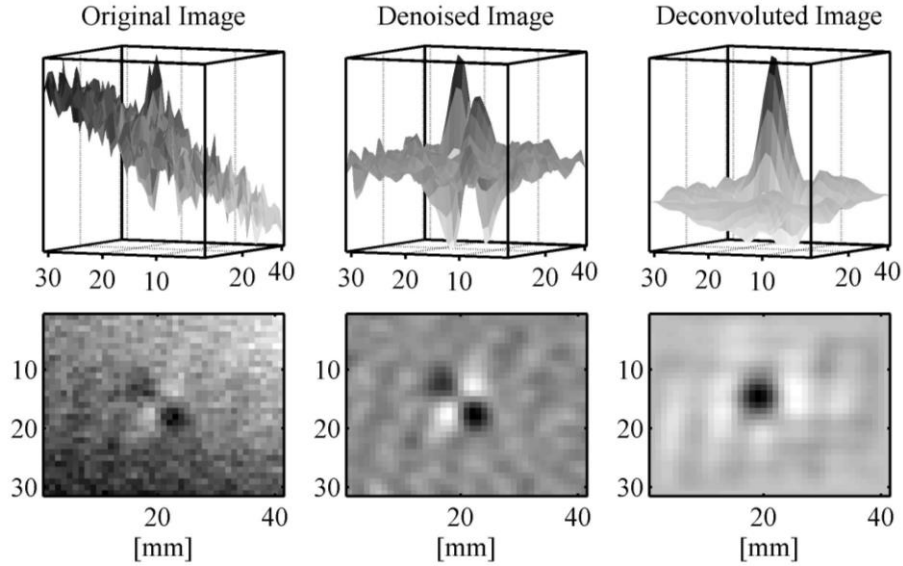


Figure 5. Example of the whole image processing procedure: starting from an image formed by raw experimental data. The denoising algorithm is initially applied to remove low-frequency and high-frequency spatial components of the noise. Subsequently a deconvolution procedure based on the HG shape is applied to enhance further the SNR and to assess better the defect location and size. The top figures represent the acquired maps while the bottom figures are the relative images converted in grayscale.

correlated with the defect depth. Except otherwise indicated, the following figures report only images obtained at f^* .

F. Hermite deconvolution

As an optional image processing step, [18] introduced the modeling of the typical quadrupolar defects pattern associated to the present measurement configuration (coil orientation + GMR orientation) with the 2D Hermite-Gauss polynomials HG(1,1) used in optics to describes intensity profiles of the modes of an optical resonator [35]. The hypothesis that patterns produced by defects can be represented by Hermite-Gauss modes of different orders HG(n,m) [36] depending on the coil orientation and on the \mathbf{B} field component measured has been further confirmed in [37].

By using this “a priori” information, a further SNR gain can be obtained when a proper deconvolution algorithm or a pattern recognition protocol is applied to the images after denoising. Since the Hermite-Gauss defect signature behaves like a Point Spread Function that blurs the “true” defect image, after deconvolution the quadri-polar pattern disappears

replaced by a peak of the intensity corresponding to the image. Moreover, noise in the images that is not in the form of Gaussian patterns is further attenuated by the deconvolution so that a higher SNR is obtained allowing the detection of defect to be improved.

An example of the whole image processing procedure is depicted in Figure 5.

IV. EXPERIMENTAL RESULTS AND COMPARISON

With the experimental set-up illustrated in Figure 1, several magnetic field maps acquired over a regular grid of $N_x=41 \times N_y=31$ measurement points with a resolution of 1mm have been acquired for various defects at the following LO values: 0.5 mm, 1.5 mm, 2.5 mm, and 3.5 mm. It is worth stressing that the GMR sensor is fixed at the bottom surface of the excitation coil so that LO refers to both the GMR and the coil distance from the sample.

In particular the comparison of the two imaging procedures has been executed on five defects, named D_1 - D_5 , consisting of subsurface cracks realized by laser ablation on a 2mm thick plate made of 2024-T3 aluminum alloy. The defects have length equal to 3mm, width of 0.1 mm and depths varying from the top surface, from 1mm to 0.2mm correspondingly with a decremental step size of 0.2mm.

A. TEST I Results with fixed lift-off

The first tests were executed by varying the lift-off of the sensor but maintaining it constant within each scan to better quantify the effect of random lift-off variation. Figure 6 shows how the $IM_{MF\bar{M}}$ and the $IM_{MF\bar{P}}$ of all the defects are modified by varying the lift-off from 0.5 to 3.5 mm. It can be seen that both imaging procedures achieve very similar results and that all the defects are clearly visible after the denoising step even at the largest value of LO . This demonstrate the good sensitivity of the whole measurement procedure, capable of detecting with high SNR a crack of $3\text{mm} \times 0.1\text{mm}$ at a depth of 1mm in a 2mm-thick plate with a LO of 3.5 mm. In addition, the plots of the $SNR(f_k)$ curves for the various defects – here not reported – show that (I) the SNR decreases as the LO increases but the descent is

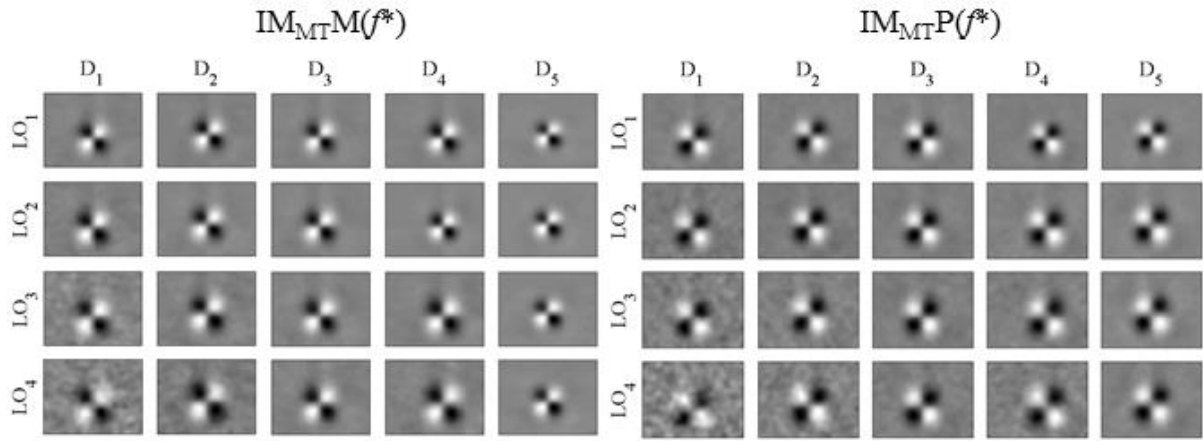


Figure 6. (left) Amplitude-based images at the optimal inspection frequency for all the defects at fixed LO values; (right) Phase-based images at the optimal inspection frequency for all the defects at fixed LO values

smooth and almost linear; (II) the amplitude-based images reach SNR values higher than the phase-based images for all the defect inspected.

B. TEST II Results in presence of lift-off variations.

The second set of tests was realized to answer the key question faced by the present work. How robust are the imaging procedures with respect to random variation of LO from point to point of a single scan?

Figure 7 reports the images obtained after denoising for all the defects with lift-off configuration LO_{R1} . It can be seen that by introducing point-by-point randomness in the lift-off value the amplitude-based images rapidly degrades (see Fig.6, rows 1 and 2 for comparison) while phase-based images remain almost unaltered and the resulting SNR is significantly higher. Similar results are obtained for the other LO configurations, as illustrated in Figure 8 where the images obtained for the deepest defects $D1$ and $D2$, for all the other LO random configurations are reported. For these defects, amplitude images do not present any HG pattern and appear as completely noisy.

Conversely, phase-based images are able to reconstruct the defects pattern even if corrupted by huge noise. As final test, we applied also HG deconvolution to the denoised images in the case of strongest “randomness” of LO , that is in configuration LO_{R4} .

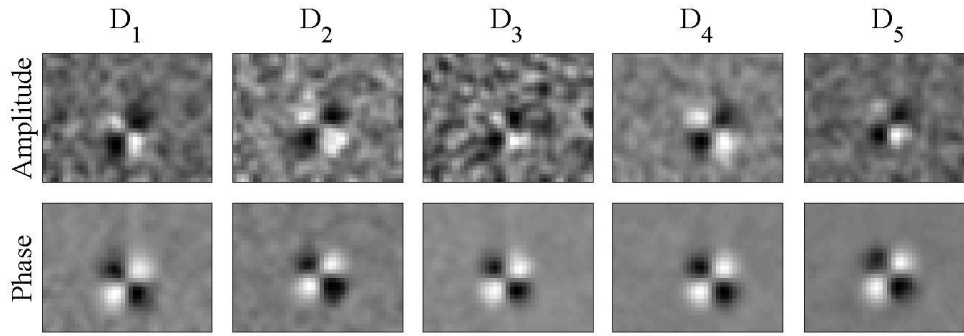


Figure 7 (top) Amplitude-based images at f^* for all the defects for LO configuration LO_{R1} ; (bottom) Phase-based images at f^* for all the defects for random LO configuration LO_{R1} .

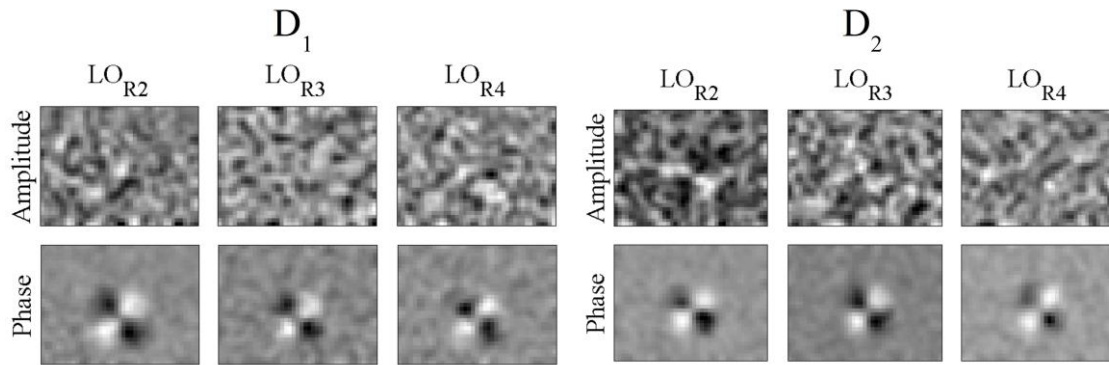


Figure 8 Images attained after denoising at f^* for random LO configurations $\{ LO_{R2}- LO_{R4} \}$: (right) defect D1; (left) defect D2

The results, reported in Figure 9, highlight the robustness of phase-based imaging with respect to lift-off variation which demonstrates that amplitude-based images are not able to detect the defects, apart from the closest one to the surface D5. Increasingly, HG deconvolution provides a significant enhancement of the SNR of the images and then a significant improvement in the defect-detection capability. It therefore contextually corroborates the Hermite-Gauss hypothesis and establishes that this procedure can help ECT sensitivity, especially in the case of low SNR. Finally, we have also analyzed the trend of $SNR(f_k)$ for amplitude and phase images for all the defects in the case of random LO - LO_{R4} configuration – to verify if optimal inspection frequency f^* is yet correlated to the defect depth.

The SNR curves for amplitude and phase are reported in Figure 10.

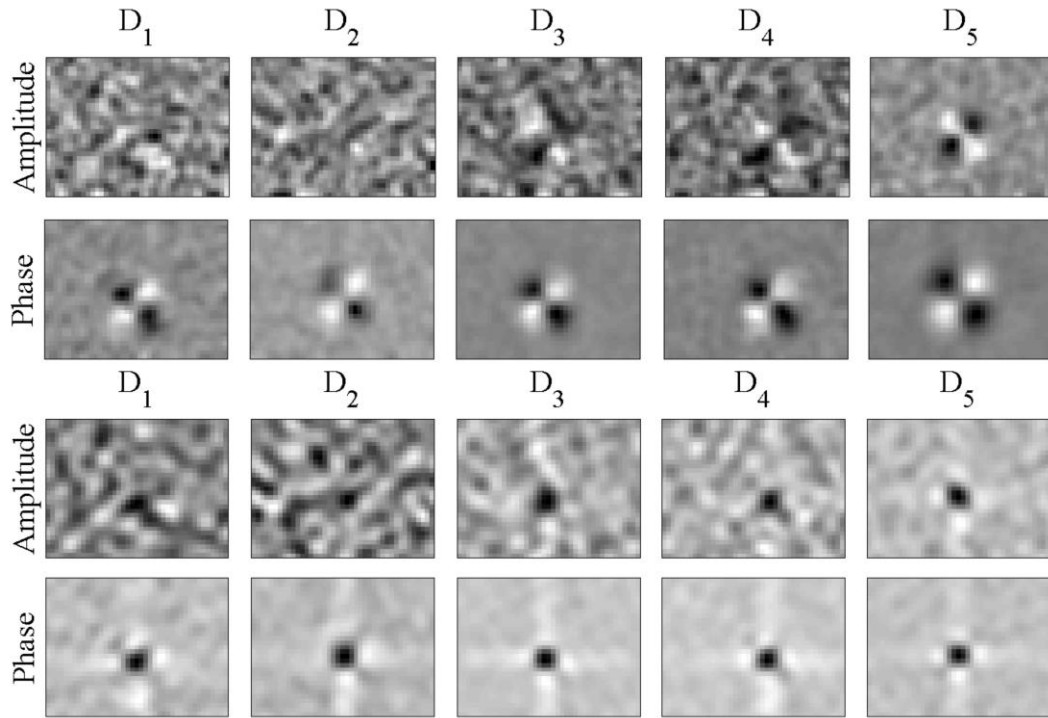


Figure 9 Images acquired at f^* for random LO configurations LO_{R4} for all the defects: (top) after denoising; (bottom) after denoising and deconvolution

It can be seen that, except for the outer defect D5, the $SNR(f_k)$ curves for IM_{MF^M} images are flat and close to the limit value ~ 3 of the SNR expected for an Additive White Gaussian Noise based on the SNR definition [18]. On the other hand, the $SNR(f_k)$ curves for IM_{MF^P} show typical trend expected also for the case of constant LO [18]. In particular it can be seen that the SNR value at the lowest frequencies is quite constant for all the defects, then increases up to the maximum value and afterwards fall down to the minimum limit value for

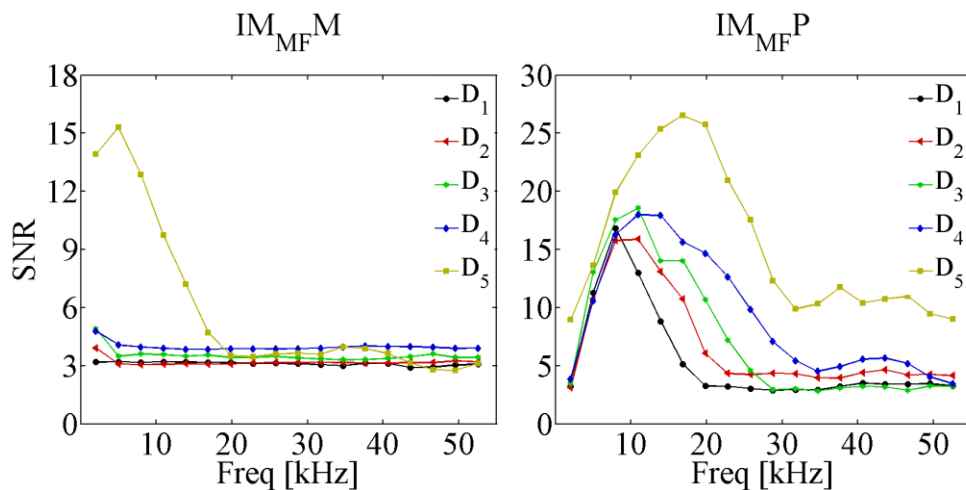


Figure 10 $SNR(f_k)$ curves obtained for all the defects in the lift-off configuration LO_{R4} : (left) amplitude-based image IM_{MF^M} (right) phase-based image IM_{MF^P}

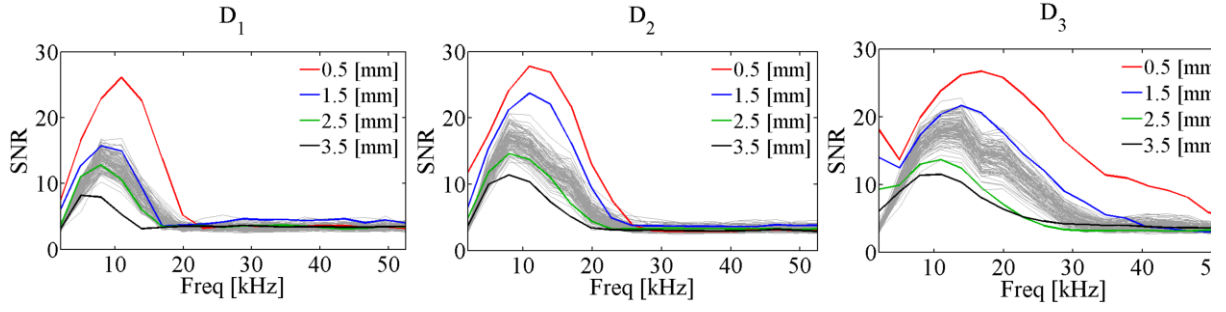


Figure 11 Comparison between $\text{SNR}(f_k)$ curves obtained at fixed lift-off (red, blue, green and black lines) and $\text{SNR}(f_k)$ curves achieved in the lift-off configuration LO_{R4} (gray lines). (left) curves for defect D1, (middle) curves for defect D2, (right) curves for defect D4

the highest frequency. The maximum of the SNR is reached at an f^* value that increases as the defect depth decreases as well as the SNR decay shifts to highest frequencies as the defect depth decreases. This is in perfect agreement with the theory and therefore the f^* is correlated with the defect depth. To further test the robustness of the phase-SNR feature with respect to lift-off variations, the simulations of point-by-point random LO variation have been repeated hundred times for each defect, analyzing the distribution of f^* and of $\text{SNR}(f^*)$. It was found that $\text{SNR}(f_k)$ trend is very stable both in amplitude and shape, then representing a good feature for experimental data. Moreover, all the $\text{SNR}(f_k)$ curves obtained for random lift-off configuration LO_{R4} fall between the curves obtained at lowest and highest LO values, nearly the center. As example, Figure 11 reports all the $\text{SNR}(f_k)$ curves obtained for defect D1, D2 and D6. The thick lines represent the $\text{SNR}(f_k)$ curves at fixed LO values, the thin gray lines report the $\text{SNR}(f_k)$ lines obtained for 100 simulations with lift-off configuration LO_{R4} .

C.TEST III Results: arbitrary random lift-off variation.

As final test, arbitrary 2D lift-off functions have been simulated by interpolating the experimental data collected at various lift-off values (see Subsection III-D). Precisely we simulated the lift-off as a sum of a point-by-point random component plus a deterministic component due to, for instance, curvature of the sample rather than misalignment of the translation stage, etc. Figure 12 illustrates the 2D surface corresponding to three among the various configuration tested and Figure 13 reports the images obtained after denoising for

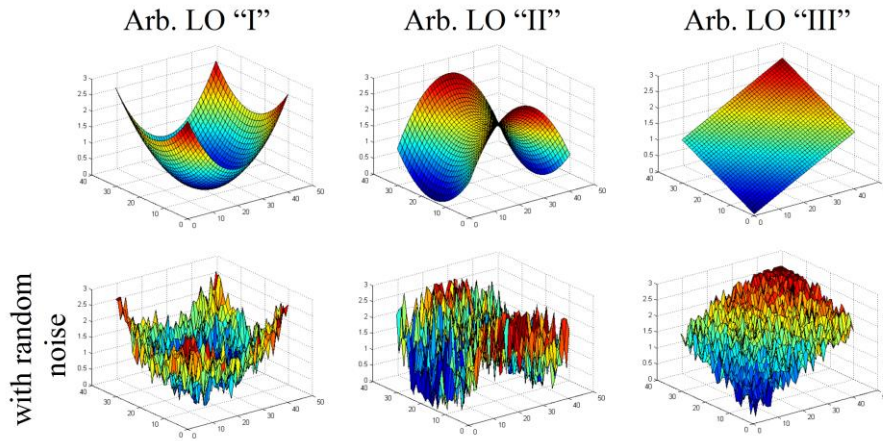


Figure 12 Simulated arbitrary 2D lift-off variations:(left) parabolic surface with point-by-point random noise, (middle) saddle-point surface with point-by-point random noise, (right) inclined plane with point-by-point random noise, these three configurations with amplitude- and phase- based imaging. It confirmed the enhanced robustness of phase with respect to change of lift-off. Finally, Figure 14 shows the $SNR(f_k)$ curves for both amplitude and phase analysis for the three arbitrary lift-off geometries. The $SNR(f_k)$ curve derived from phase-images remains “well-behaved” as for random variation.

CONCLUSIONS

A thorough comparison of eddy current imaging procedures based on amplitude and phase analysis has been executed on experimental data collected by using multi-frequency excitation on different defects in presence of variable lift-offs. The obtained imaging results have been quantitatively compared by means of a suitable SNR-merit factor that allows the evaluation of the image quality. A number of experiments have shown how lift-off variations affect the SNR and hence the image quality, allowing or not the detection of the defect investigated. It has been found that images derived from phase analysis are extremely robust with respect to lift-off variations. Conversely, images derived from amplitude analysis; though achieve higher SNR’s for fixed lift-off, are very sensitive to fluctuations of the lift-off. This lift-off insensitivity of SNR evaluated on the phase together with its frequency behavior on the different defects seems to be a robust feature from which information about the defect depth can be inferred.

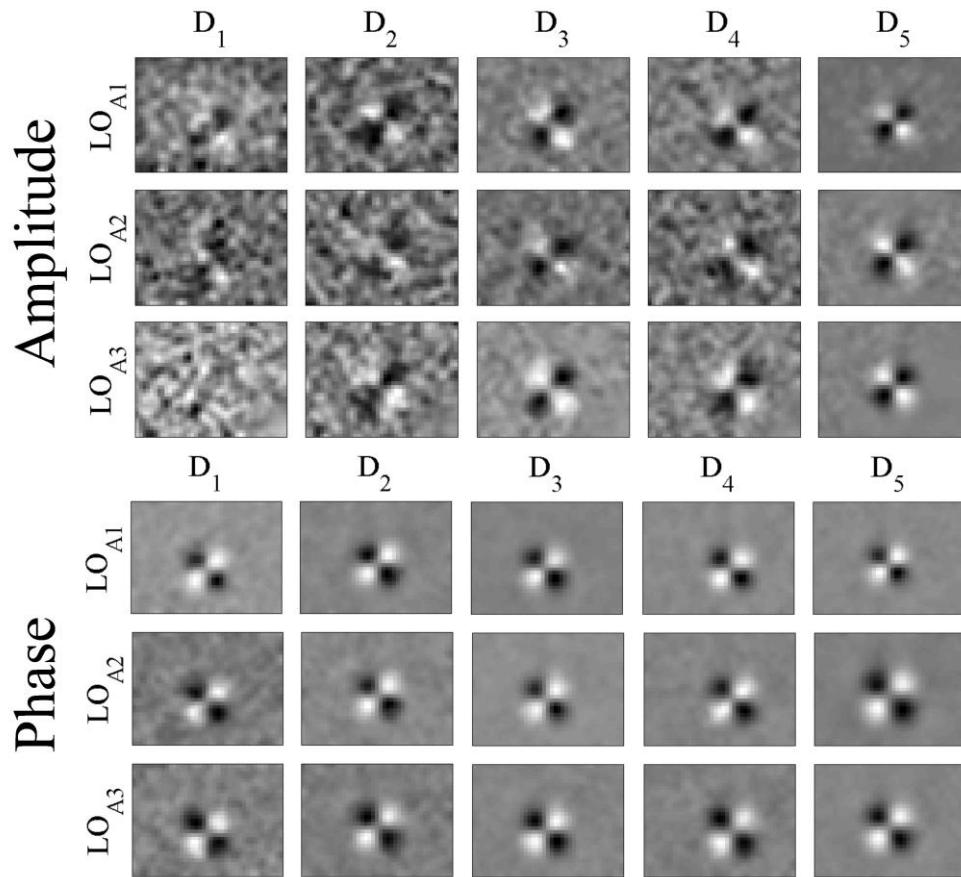


Figure 13 Images attained at f^* for arbitrary LO configurations for all the defects: (left) amplitude analysis, (right) phase analysis

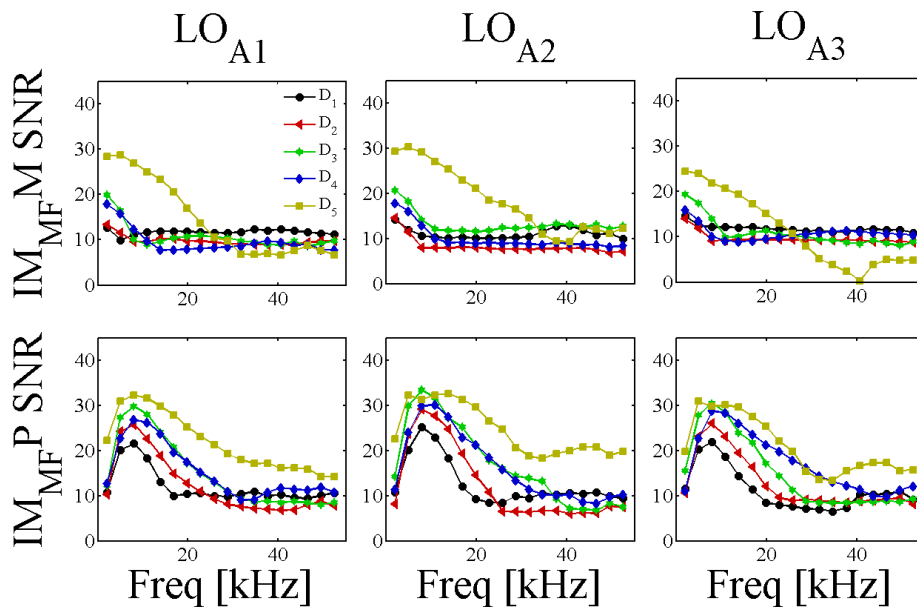


Figure 14 Comparison between $SNR(f_k)$ curves obtained for the three arbitrary lift-off variations with (top) amplitude and (bottom) phase analysis.

ACKNOWLEDGMENTS

M.R., G.S. and I.A. acknowledge financial support from Fondazione Carit “Tecniche elettromagnetiche per il controllo di saldature in strutture metalliche complesse”

REFERENCES

- [1] B. Lebrun, Y. Jayet, J.C. Baboux, (1997). Pulsed eddy current signal analysis: application to the experimental detection and characterization of deep flaws in highly conductive materials. *NDT & e international*, 30(3), 163-170.
- [2] Sophian, A., Tian, G. Y., Taylor, D., & Rudlin, J. (2002). Design of a pulsed eddy current sensor for detection of defects in aircraft lap-joints. *Sensors and Actuators A: Physical*, 101(1), 92-98.
- [3] G. Yang, *et al.* (2010). Pulsed eddy-current based giant magnetoresistive system for the inspection of aircraft structures. *Magnetics, IEEE Transactions on*, 46(3), 910-917.
- [4] P. Horan, *et al.* (2013). Pulsed eddy current detection of cracks in F/A-18 inner wing spar without wing skin removal using Modified Principal Component Analysis. *NDT & E International*, 55, 21-27.
- [5] Mook, G., Lange, R., & Koeser, O. (2001). Non-destructive characterisation of carbon-fibre-reinforced plastics by means of eddy-currents. *Composites science and technology*, 61(6), 865-873.
- [6] Yin, W., Withers, P. J., Sharma, U., & Peyton, A. J. (2009). Noncontact characterization of carbon-fiber-reinforced plastics using multifrequency eddy current sensors. *Instrumentation and Measurement, IEEE Transactions on*, 58(3), 738-743.
- [7] Vrana, J., et al. (2008). Mechanisms and models for crack detection with induction thermography. *AIP Proceedings (Vol. 975, No. 1, p. 475)*.
- [8] He, Y., Tian, G., Pan, M., & Chen, D. (2014). Impact evaluation in carbon fiber reinforced plastic (CFRP) laminates using eddy current pulsed thermography. *Composite Structures*, 109, 1-7.
- [9] Weekes, Ben, et al. "Eddy-current induced thermography—probability of detection study of small fatigue cracks in steel, titanium and nickel-based superalloy." *NDT & E International* 49 (2012): 47-56.
- [10] Washabaugh, A., et al. (2012). *NDT and SHM of Carbon Fiber Composites using Linear Drive MWM-Arrays*.
- [11] Le Diraison, Y., Joubert, P. Y., & Placko, D. (2009). Characterization of subsurface defects in aeronautical riveted lap-joints using multi-frequency eddy current imaging. *NDT & E International*, 42(2), 133-140.

- [12] Postolache, O., Ribeiro, A. L., & Ramos, H. G. (2013). GMR array uniform eddy current probe for defect detection in conductive specimens. *Measurement*, 46(10), 4369-4378.
- [13] Tian, G. Y., & Sophian, A. (2005). Reduction of lift-off effects for pulsed eddy current NDT. *NDT & E International*, 38(4), 319-324.
- [14] Ribeiro, A. L., Ramos, H. G., & Arez, J. C. (2012). Liftoff insensitive thickness measurement of aluminum plates using harmonic eddy current excitation and a GMR sensor. *Measurement*, 45(9), 2246-2253.
- [15] G.Y. Tian, Y. He, I. Adewale, A. Simm, (2013). Research on spectral response of pulsed eddy current and NDE applications. *Sensors and Actuators A: Physical*, 189, 313-320.
- [16] I.D. Adewale, G.Y. Tian, Song HuaDong (2015) : "Separation of lift-off and defect depth features in magnetic-sensor based Pulsed Eddy Current Signals," *Electromagnetic Nondestructive Evaluation (XVIII)*, 40, 211-221.
- [17] A. Bernieri, G. Betta, L. Ferrigno, M. Laracca, S. Mastrostefano, "Multifrequency excitation and support vector machine regressor for ECT defect characterization", *IEEE Transactions on Instrumentation and Measurement*, Vol. 63 (5), pp. 1272-1280, 2014
- [18] Betta, Giovanni, Luigi Ferrigno, Marco Laracca, Pietro Burrascano, Marco Ricci, and Giuseppe Silipigni. "An experimental comparison of multi-frequency and chirp excitations for eddy current testing on thin defects." *Measurement* 63 (2015): 207-220.
- [19] Chady, T., Enokizono, M., & Sikora, R. (1999). Crack detection and recognition using an eddy current differential probe. *Magnetics, IEEE Transactions on*, 35(3), 1849-1852.
- [20] Glorieux, C., Moulder, J., Basart, J., & Thoen, J. (1999). The determination of electrical conductivity profiles using neural network inversion of multi-frequency eddy-current data. *Journal of Physics D: Applied Physics*, 32(5), 616.
- [21] He, D. F., M. Shiwa, J. P. Jia, J. Takatsubo, and S. Moriya. "Multi-frequency ECT with AMR sensor." *NDT & E International* 44, no. 5 (2011): 438-441.
- [22] Udpa, L., and W. Lord. "Diffusion, waves, phase and eddy current imaging." In *Review of Progress in Quantitative Nondestructive Evaluation*, pp. 499-506. Springer US, 1985.
- [23] Edwards, John, and Tapan K. Saha. "Diffusion of current into conductors." In *Australasian Universities Power Engineering Conference*, vol. 1, pp. 401-406. CRESTA, 2001.
- [24] Kreutzbruck, M., Allweins, K., Rühl, T., Mück, M., Heiden, C., Krause, H. J., & Hohmann, R. (2001). Defect detection and classification using a SQUID based multiple frequency eddy current NDE system. *Applied Superconductivity, IEEE Transactions on*, 11(1), 1032-1037.
- [25] Sikora, R., Chady, T., Gratkowski, S., Komorowski, M., & Stawicki, K. (2003, March). Eddy current testing of thick aluminum plates with hidden cracks. *AIP Conference Proceedings (No. A, pp. 427-434)*. IOP INSTITUTE OF PHYSICS PUBLISHING LTD.

- [26] Ricci M., Silipigni G.; Ferrigno L., Laracca M., Adewale, I.D., Gui Yun Tian, "Analysis of the influence of lift-off variation on Eddy-Current images", proceedings of IEEE Metrology for Aerospace (MetroAeroSpace), 4-5 June 2015, Benevento (Italy), pp. 182-187.
- [27] Le Bihan, Yann. "Study on the transformer equivalent circuit of eddy current nondestructive evaluation." *NDT & E International* 36, no. 5 (2003): 297-302.
- [28] Le Bihan, Y. "Lift-off and tilt effects on eddy current sensor measurements: a 3-D finite element study." *The European Physical Journal Applied Physics* 17, no. 01 (2002): 25-28.
- [29] Zhang, Yu-hua, Fei-lu Luo, and Hui-xian Sun. "Impedance evaluation of a probe-coil's lift-off and tilt effect in eddy-current nondestructive inspection by 3D finite element modeling." In *17th World Conference on Nondestructive Testing*. 2008.
- [30] Ribeiro, A. Lopes, H. Geirinhas Ramos, and J. Couto Arez. "Liftoff insensitive thickness measurement of aluminum plates using harmonic eddy current excitation and a GMR sensor." *Measurement* 45, no. 9 (2012): 2246-2253.
- [31] Yin, Wuliang, Richard Binns, Stephen J. Dickinson, Claire Davis, and Anthony J. Peyton. "Analysis of the liftoff effect of phase spectra for eddy current sensors." *Instrumentation and Measurement, IEEE Transactions on* 56, no. 6 (2007): 2775-2781.
- [32] Yin, W.; Xu, K., "A Novel Triple-Coil Electromagnetic Sensor for Thickness Measurement Immune to Lift-Off Variations," in *Instrumentation and Measurement, IEEE Transactions on*, vol. PP, no. 99, pp. 1-6 (2015)
- [33] M. R. Schroeder, "Synthesis of Low-Peak-Factor Signals and Binary Sequences with Low Autocorrelation", *IEEE Transactions on Information Theory* Vol. 16, Issue 1, pp. 85-89, 1970.
- [34] Ricci, Marco, Luca Senni, and Pietro Burrascano. "Exploiting pseudorandom sequences to enhance noise immunity for air-coupled ultrasonic nondestructive testing." *Instrumentation and Measurement, IEEE Transactions on* 61, no. 11 (2012): 2905-2915.
- [35] Kogelnik, H., and Tingye Li. "Laser beams and resonators." *Applied Optics* 5, no. 10, 1550-1567 (1966)
- [36] Hermite-Gaussian beams are similar to Gaussian ones, except that the electric field amplitude is modulated in the transverse direction according to:

$$E(x, y) = AH_l \left(\frac{\sqrt{2}}{w} x \right) H_m \left(\frac{\sqrt{2}}{w} y \right) e^{-\frac{(x^2+y^2)}{w^2}}$$

where w is the spot size at the position z , and the $H_m(u)$ are Hermite polynomials. For our purpose, it is sufficient to know that these are well-known polynomials of order m , which are the solution to a particular differential equation. For example, these functions turn up in the solution of the harmonic oscillator problem in quantum mechanics. The first few Hermite polynomials are: $H_0(u)=1$, $H_1(u)=2u$, $H_2(u)=4u^2-2$, $H_3(u)=8u^3-12u$.

- [37] Betta, G., L. Ferrigno, M. Laracca, H. G. Ramos, M. Ricci, A. L. Ribeiro, and G. Silipigni. "Fast 2D crack profile reconstruction by image processing for Eddy-Current Testing." In *Metrology for Aerospace (MetroAeroSpace)*, 2015 IEEE, pp. 341-345. IEEE, 2015.